Published in final edited form as:

Biomacromolecules. 2019 January 14; 20(1): 469–477. doi:10.1021/acs.biomac.8b01365.

Biodistribution of Filamentous Plant Virus Nanoparticles: Pepino Mosaic Virus versus Potato Virus X

Duc H. T. Le[⊥,¶], **Eduardo Méndez-López**[#], **Chao Wang**[†,⊥], **Ulrich Commandeur**[▽], **Miguel A. Aranda**[#], and **Nicole F. Steinmetz**[*,†,§,‡,‖,⊥]

[†]Department of NanoEngineering, University of California, San Diego, La Jolla, California 92093, United States

[‡]Moores Cancer Center, University of California, San Diego, La Jolla, California 92093, United States

[§]Department of Radiology, University of California, San Diego, La Jolla, California 92093, United States

[‖]Department of Bioengineering, University of California, San Diego, La Jolla, California 92093, United States

[⊥]Department of Biomedical Engineering, Case Western Reserve University School of Medicine, Cleveland, Ohio 44106, United States

[#]Centro de Edafología y Biología Aplicada del Segura (CEBAS)-CSIC, Campus Universitario de Espinardo, 30100 Murcia, Spain

[▽]Department of Molecular Biology, RWTH-Aachen University, Aachen 52064, Germany

Abstract

Nanoparticles with high aspect ratios have favorable attributes for drug delivery and bioimaging applications based on their enhanced tissue penetration and tumor homing properties. Here, we investigated a novel filamentous viral nanoparticle (VNP) based on the Pepino mosaic virus (PepMV), a relative of the established platform Potato virus X (PVX). We studied the chemical reactivity of PepMV, produced fluorescent versions of PepMV and PVX, and then evaluated their biodistribution in mouse tumor models. We found that PepMV can be conjugated to various small chemical modifiers including fluorescent probes via the amine groups of surface-exposed lysine

[*]**Corresponding Author** nsteinmetz@ucsd.edu.

[¶]**Present Address** Eindhoven University of Technology, P.O. Box 513 (STO 3.25), 5600MB Eindhoven, The Netherlands; Department of Biochemistry, Radboudumc, Geert Grooteplein 28, 6525 GA Nijmegen, The Netherlands.

Author Contributions

E.M.-L. and M.A.A. provided PepMV. U.C. provided PVX. D.H.T.L. performed bioconjugation, nanoparticle characterization, and the biodistribution study in the mouse model of triple negative breast cancer. D.H.T.L. and C.W. performed the biodistribution study in the mouse model of ovarian cancer. D.H.T.L. analyzed the data. D.H.T.L. and N.F.S. wrote the manuscript. N.F.S. conceived, designed, and oversaw the study. All authors read and approved the manuscript.

Supporting Information

The Supporting Information is available free of charge on the ACS Publications Web site. ACS Publications website at DOI: 10.1021/acs.biomac.8b01365.

The sequences of PepMV and PVX, hydropathy plots of the first 20 amino acids of PepMV and PVX (Figure S1), and a summary table showing differences in the N-terminal peptide tails of PepMV and PXV (Table S1) (PDF)

The authors declare no competing financial interest.

residues, yielding VNPs carrying payloads of up to 1600 modifiers per particle. Although PepMV and PVX share similarities in particle size and shape, PepMV achieved enhanced tumor homing and less nonspecific tissue distribution compared to PVX in mouse models of triple negative breast cancer and ovarian cancer. In conclusion, PepMV provides a novel tool for nanomedical research but more research is needed to fully exploit the potential of plant VNPs for health applications.

Graphical abstract

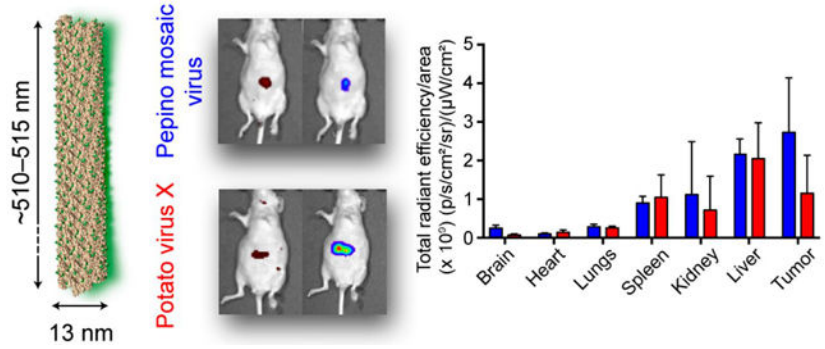

INTRODUCTION

The next generation of nanotechnology-based imaging agents and drugs offers new opportunities in both fundamental and clinical research.[1,2] State-of-the-art chemistries allow the fabrication of nanoparticles with a diverse portfolio of shapes and sizes, enabling the development of designer nanoparticles suitable for many different applications. While small molecule therapeutics and contrast agents suffer from poor solubility, rapid clearance, and nonspecific tissue distribution, nanoparticles have the potential to overcome these shortcomings. However, more research is needed to identify novel platforms that can facilitate effective drug delivery and imaging beyond applications in cell culture and animal models. Although polymeric nanoparticles and liposomal drug formulations have received significant attention, biological nanomaterials offer advantages such as the biomanufacturing and self-replication of biological systems, leading to high-precision nanotechnologies. We have therefore focused on the development of plant virus-based nanotechnologies as next-generation biologicals.[3,4]

Viral nanoparticles (VNPs) are simple nanoscale structures consisting of a genome and a proteinaceous coat that is self-assembled from coat proteins (CPs). Programmed by nature, these nanostructures are diverse in terms of size (10–500 nm) and shape (icosahedrons, rods, filaments, or more complex head-to-tail architectures).[3] Their advantages include homogeneity and monodispersity, resulting in a high degree of quality control that is critical for clinical translation. We have focused on plant VNPs because they are biocompatible, biodegradable, and noninfectious in mammals and can be produced in large quantities by molecular farming with high yields and excellent reproducibility. Among several plant VNPs under development, the chemistry and in vivo properties of the Cowpea mosaic virus (CPMV), a 30 nm icosahedral particle, are particularly well understood. CPMV has been used for drug delivery,[5] imaging,[6] vaccine development,[7] and immunotherapy applications.[8]

Other icosahedral plant VNPs have been developed from the Cucumber mosaic virus (CMV),[9] the Physalis mottle virus (PhMV),[10] and the Red clover necrotic mottle virus (RCNMV).[11]

In addition to the icosahedral viruses described above, high-aspect-ratio, soft-matter nanotubes formed by the Tobacco mosaic virus (TMV) have also been used for drug delivery[12–14], imaging[15,16], vaccine development [17–19], and cancer immunotherapy.[20] Similarly, the filamentous particles formed by the Potato virus X (PVX) have been explored for the same broad panel of applications.[21–24] Structure—function studies have highlighted the importance of nanoparticle shape. In our previous work, we found that filamentous PVX (515 × 13 nm) and icosahedral CPMV (30 nm) differ in their biodistribution profiles, with PVX demonstrating enhanced tumor homing and tissue penetration.[23,25] These observations are matched with data from studies using synthetic nanomaterials such as carbon nanotubes and filomicelles [26,27] confirming that a high aspect ratio is advantageous for nanomedical applications because the particles evade phagocytosis, leading to prolonged circulation time while also exhibiting enhanced margination and extravasation thus facilitating homing and accumulation at tumor sites.[28–30]

Given the encouraging data with the filamentous PVX platform,[21–24] we have expanded our research to include other filamentous plant viruses because each platform is different in terms of its material properties, chemistry, suitability for engineering, and in vivo fate. We therefore compared the properties of PVX and the Pepino mosaic virus (PepMV), a common pathogen that infects tomato plants.[31–33] A stable PepMV vector was recently generated to support biomanufacturing.[32] PepMV and PVX both belong to the genus *Potexvirus* in the family *Flexiviridae.* They share filamentous nucleoprotein architectures assembled from helically arranged CP subunits around their single-stranded, positive-sense RNAs. The PepMV virion is constructed from 1290 identical CPs to form a 510 × 13 nm filament very similar to the 515 × 13 nm PVX virion comprising 1270 identical CPs. The PVX particle offers addressable lysine (Lys) and cysteine (Cys) side chains, allowing the preparation of the multimodal nanotechnology platform.[34] We used the available three-dimensional (3D) structural model of PepMV to identify chemically addressable Lys side chains and to establish bioconjugation procedures. We developed PepMV with small chemical modifiers such as a biotin tag and a fluorescent probe. The in vivo fate of fluorescence-labeled PepMV in terms of biodistribution and tumor homing properties was then compared in mouse models of triple negative breast cancer and ovarian cancer.

MATERIALS AND METHODS

Preparation of the Filamentous VNPs.

PepMV and PVX were propagated in *Nicotiana benthamiana* plants and purified according to our established protocols.[33,35] The yields from 100 g of infected leaves were ~10 to 20 mg of pure PepMV and PVX.

Structural Models of the Filamentous VNPs.

The atomic model and cryoEM structure of the PepMV CP were generated using UCSF Chimera with data imported from the Protein Data Bank (PDB 5FN1). The atomic model ofthe PVX CP (NCBI AAV27212.1) was constructed using the Rosetta web server by comparative modeling based on the PepMV atomic model. The PVX and PepMV CPs share 53% sequence similarity and 37% sequence identity.[34] The assembled structure of PVX was generated by fitting the PepMV model in UCSF Chimera, assuming similar helical symmetry parameters. Addressable Lys was depicted in green from the top, side, and bottom of the VNP models. Surface charge densities were calculated using the Bluues server (http://protein.bio.unipd.it/bluues) on the basis of generalized Born radii.[36]

Chemical Bioconjugation of the VNPs.

Biotin *N*-hydroxysuccinimide ester (Biotin-NHS) and sulfo-Cyanine5 NHS (Cy5-NHS) were obtained from Medchem Express and Lumiprobe, respectively. For amine-NHS coupling, mixtures of VNPs (2 mg mL^{-1}) with the NHS reagents were prepared in 10 mM potassium phosphate (KP) buffer containing 10% (v/v) DMSO (pH 7.0). All reactions were carried out at room temperature overnight. Biotin-NHS was added at a 1:1 molar ratio with the CP. Cy5-NHS was added at increasing CP/dye ratios of 1:1, 1:2, 1:5, 1:10, and 1:20. Biotinylated PepMV and PVX were purified by 10 washes in 10 mM KP buffer, using 100-kDa molecular weight cutoff size exclusion spin filters. For fluorescence-labeled particles, the PepMV-Cy5 and PVX-Cy5 conjugates were purified by three rounds of ultracentrifugation (112,000 × *g*, 1 h, 4 °C) over a 30% (w/v) sucrose cushion. The pellets were then resuspended in 10 mM KP buffer, pH 7.0.

Denaturing Gel Electrophoresis (SDS-PAGE).

Denatured samples (5 μg) were loaded onto 4–12% NuPAGE gels (Thermo Fisher Scientific) in 1× MOPS running buffer (Thermo Fisher Scientific). Electrophoresis was conducted at a constant voltage (200 V) for 35 min. Labeled samples were detected by excitation at 632 nm (red) and imaged using the FluoroChem R imaging instrument (ProteinSimple). After staining with Coomassie Blue (CB), protein bands were visualized under white light and imaged using the same equipment.

Western Blot (WB) Analysis.

After SDS-PAGE, the separated capsid bands were then transferred from gels onto a nitrocellulose membrane (Thermo Fisher Scientific) and blocked for 60 min using 5% (w/v) skimmed milk powder dissolved in 0.1 M Tris-buffered saline containing 0.05% (v/v) Tween-20 (TBST). Alkaline phosphatase-conjugated streptavidin (Sigma-Aldrich) diluted in 5% (w/v) milk in TBST at a 1:500 ratio was used to detect the biotinylated samples. BCIP/NBT substrate for alkaline phosphatase was added for visualization. Imaging was carried out using the FluoroChem R imaging instrument.

Transmission Electron Microscopy (TEM) Imaging.

Samples (0.1 mg mL^{-1}) were loaded onto carbon-coated grids and negatively stained with 0.2% (w/v) uranyl acetate. Grids were imaged using a FEI Tecnai F30 transmission electron microscope operated at 300 kV.

Immunogold Staining for the Detection of Biotinylated VNPs.

Samples loaded on carbon-coated grids were washed with 10 mM KP buffer and blocked with 1% (w/v) bovine serum albumin (BSA) containing 0.1% (v/v) Tween-20 for 30 min. After equilibration in 0.1% (w/v) BSA for 5 min, the samples were stained with 10 nm gold nanoparticles conjugated to antibiotin antibodies (AURION) diluted 5-fold in KP buffer. Finally, the samples were negatively stained using 2% (w/v) uranyl acetate for 1 min prior to TEM imaging using a FEI Tecnai F30 transmission electron microscope at 300 kV.

UV/vis Spectroscopy.

A Nanodrop 2000 spectrometer (Thermo Fisher Scientific) was used to measure the absorbance at 260 nm (for viral RNAs) to determine the VNP concentration and the absorbance at 647 nm to determine the concentration of attached dyes after purification. Using the Beer—Lambert law and extinction coefficients specific for PepMV (2.9 mL mg^{-1} cm^{-1}), PVX (3.0 mL mg^{-1} cm^{-1}), and Cy5 (271,000 M^{-1} cm^{-1}), the molar ratios of conjugated dyes per particle were calculated. Triplicate samples were prepared, and data were expressed as means ± SD. Statistical significance was determined by applying a *t* test in GraphPad Prism.

Biodistribution Studies.

To track the filamentous VNPs in vivo, PepMV and PVX were labeled with Cy5 as above using CP/dye ratios for PepMV and PVX optimized at 1:0.4 and 1:1, respectively, ensuring ~300 dye molecules per particle in both cases. Purification was then carried out by two rounds of ultracentrifugation (212,000 × *g*, 3 h, 4 °C). The filamentous structures of PepMV-Cy5 and PVX-Cy5 were confirmed by TEM before in vivo administration. All animal studies were conducted following the protocols and procedures approved by Case Western Reserve University's Institutional Animal Care and Use Committee. Athymic female NCR *nu/nu* mice (6–8 weeks old, obtained from Case Western Reserve University) were fed on an alfalfa-free diet to reduce autofluorescence. For the triple negative breast cancer (TNBC) model, mice (6–8 weeks old) were injected subcutaneously in the right flank with 2×10^6 cells suspended in 100 μL 1:1 Matrigel/medium. Tumor volumes were monitored daily and calculated using the formula $v = (l \times w^2)/2$ where l is the length and w is the width of a tumor. Biodistribution was analyzed when the tumor volume reached 100–150 mm^3. PepMV-Cy5 and PVX-Cy5 were administered intravenously at a dose of 10 mg kg^{-1} body weight. Mice were euthanized, and organs were collected for ex vivo imaging using the IVIS spectrum imaging system (PerkinElmer Ltd.) 24 h post injection. Regions of interest (ROI) were analyzed using the IVIS Living Image v4.2 (PerkinElmer Ltd.) to determine the fluorescence intensity per area from each organ. Data were expressed as means ± SD ($n = 3$). Similarly, for the ovarian cancer model, luciferase-positive SKOV-3/Luc cells (2×10^6 cells in 0.2 mL PBS) were injected intraperitoneally (i.p.) and tumor growth was monitored

weekly by bioluminescence imaging following the injection of D-luciferin (Thermo Fisher Scientific) at a dose of 150 mg kg^{-1}. The total luminescence intensity was determined by ROI analysis. After 40 days, mice were injected i.p. with PepMV-Cy5 and PVX-Cy5 at a dose of 10 mg kg^{-1} body weight. The VNP distribution was monitored in vivo using the IVIS system under isoflurane anesthesia at defined time points for 72 h. Organs were collected and imaged ex vivo, and ROI analysis was conducted as described above. Quantitative data were expressed as means ± SD (n = 3).

RESULTS AND DISCUSSION

Mapping of Addressable Lys Side Chains on the Filamentous VNPs.

To explore the available engineering design space of the VNPs, the three-dimensional (3D) structures of PepMV and PVX were constructed using UCSF Chimera software (Figure 1). The PepMV and PVX CP atomic models with all Lys side chains (amino groups highlighted in green) are shown in parts A and B of Figure 1, respectively. The corresponding assembled nanoparticles are shown in parts C and D of Figure 1, respectively, illustrating the surface-exposed Lys from different angles. In addition, the electrostatic potentials of the solvent-exposed surfaces on each VNP were calculated using the Bluues server, indicating that each assembled CP featured a negatively charged surface (Figures 1E,F). There are 13 Lys residues in the PepMV CP and 11 in the PVX CP, as shown in parts A and B of Figure 1, respectively. The structural model of PepMV (Figure 1C), viewed from the side, indicates that Lys 41, 42, 44, 63, and 18 are fully exposed (Lys 18 is not shown; the first 20 residues are solvent-exposed but not included in the atomic models because the lack of electron density indicates a flexible structure). Lys 23, 132, and 158 are partially buried in the surface, and Lys 93, 187, and 204 face the CP interfaces and are therefore only exposed at the ends. Finally, Lys 150 and 196 are buried in the CP structure (Figure 1C). The PVX structural model indicates five fully exposed Lys residues (20, 61, 67, 71, and 177) as well as the partially exposed Lys 118 (Figure 1D). Lys 154 and 158 face the CP interfaces and are therefore exposed only at the end structures of the PVX virion (Figure 1D). The structural data thus indicate that both PepMV and PVX have several solvent-exposed Lys side chains.

Bioconjugation of PepMV and PVX.

Next, we compared the versatility of PepMV and PVX by testing a series of bioconjugation chemistries (Figures 2 and 3). We previously demonstrated that PVX could be labeled on solvent-exposed Lys side chains with small chemical modifiers using *N*-hydroxysuccinimide (NHS) esters.[34] Up to 1600 modifiers (e.g., Oregon green 488) could be displayed per particle, indicating that each of the 1270 identical CP copies could accommodate one or two conjugated molecules. Here, we used similar bioconjugation procedures to test the chemistry of PepMV, namely NHS esters of biotin and sulfo-Cyanine 5 fluorophores (Scheme 1).

First, we tested the biotinylation of Lys side chains on the filamentous VNPs (Figure 2). PepMV or PVX suspensions at a final concentration of 2 mg mL^{-1} were mixed with biotin-NHS at a 1:1 CP/biotin-NHS ratio in 10 mM potassium phosphate (KP) buffer (pH 7.0) containing 10% (v/v) DMSO at room temperature overnight. The biotinylated conjugates (PepMV-biotin and PVX-biotin) were then purified using 100 kDa molecular weight cutoff

spin filters (10 washes with 10 mM KP buffer) to remove excess biotin. SDS-PAGE and Western blot analysis confirmed the successful biotinylation of both viruses (Figure 2A). SDS-PAGE revealed a ~25 kDa band representing the PepMV and PVX CP, but no increase in molecular weight was observed following the conjugation reaction due to the small size of biotin (244 Da). Nevertheless, Western blots probed with alkaline phosphatase-conjugated streptavidin confirmed the presence of the biotin tag. Immunogold-TEM imaging using an antibiotin antibody conjugated with 10 nm gold nanoparticles also confirmed that PepMV and PVX were coated with biotin and that the VNPs preserved their flexuous, filamentous structures after bioconjugation and purification, as shown in parts B and C of Figure 2.

Next, we used a fluorescent label (sulfo-Cyanine 5 NHS, Cy5-NHS) to quantify the loading capacity of PepMV (Figure 3). PepMV and PVX particle suspensions (2 mg mL^{-1}) were mixed with Cy5-NHS at 1:1, 1:2, 1:5, 1:10, and 1:20 CP/Cy5-NHS ratios. The reactions were carried out at room temperature overnight, followed by three rounds of ultracentrifugation (112,000 × *g*, 1 h, 4 °C) to remove excess dye. After SDS-PAGE, the gels were first visualized by excitation at 632 nm (red) to detect conjugated Cy5 (Ex/Em 647/662 nm) (Figures 3A,B). In contrast to the nonmodified CPs, the Cy5-conjugated CPs were fluorescent, indicating that both PepMV and PVX were successfully labeled (Figures 3A,B). TEM imaging confirmed that PepMV and PVX (prepared using a Cy5-NHS/CP ratio of 1:1) remained intact after the labeling and purification procedure (Figure 3C). Next, we determined the number of Cy5 dye molecules attached per PepMV or PVX particle by UV/vis spectroscopy using the Beer–Lambert law and the specific extinction coefficients of PepMV (2.9 mL mg^{-1} cm^{-1} at 260 nm), PVX (3.0 mL mg^{-1} cm^{-1} at 260 nm), and Cy5 (271,000 M^{-1} cm^{-1} at 647 nm). As shown in Figure 3D, more dye molecules are conjugated as the molar excess of dye increases. The reaction reached a plateau with conjugation efficiencies of 1600 Cy5 per PepMV and 1100 Cy5 per PVX using the 1:20 CP/Cy5-NHS ratio. Under each condition tested, PepMV showed a higher loading capacity than PVX ($p < 0.001$, *t* test in GraphPad Prism). The slightly higher loading capacity of PepMV may reflect the larger number of solvent-exposed Lys side chains that are accessible during the conjugation reaction.

Biodistribution Studies.

To investigate the potential of PepMV for drug delivery and/or diagnostic imaging applications, we carried out biodistribution studies using two mouse models: a *nu/nu* mouse model of TNBC using subcutaneously inoculated MDA-MB-231 cells and a model of ovarian cancer using intraperitoneally inoculated SKOV-3 cells. All animal studies were conducted according to Case Western Reserve University IACUC-approved protocols. To monitor the nanoparticles in vivo and ex vivo, PepMV-Cy5 and PVX-Cy5 were prepared using reaction conditions that ensured each particle was labeled with ~300 dye molecules, which is suitable for imaging without quenching effects. Free dye was removed by ultracentrifugation, and the integrity of the filamentous particles was confirmed by TEM before injection. The number of PepMV and PVX particles in animal tissues was determined indirectly by measuring the fluorescence intensity. PepMV-Cy5 and PVX-Cy5 (10 mg kg^{-1} body weight) were administered intravenously (i.v.) to female mice bearing MDA-MB-231 tumors or intraperitoneally (i.p.) to mice bearing SKOV-3 tumors. In vivo and ex vivo

imaging was performed using an IVIS spectrum imaging system, followed by the quantitative analysis of fluorescence in each organ (ROI analysis) using Living Imaging Software (Figures 4 and 5). One-way analysis of variance (ANOVA) in GraphPad Prism was used to determine the statistical significance of differences between tissues, and *t* tests were similarly used for pairwise comparisons between PepMV and PVX in each tissue.

For the TNBC model, MDA-MB-231 cells were inoculated subcutaneously at a concentration of 2×10^6 cells mL^{-1} in the right flank of female *nu/nu* mice. After 14 days, when tumor volumes reached 100–150 mm^3, mice were divided into two groups for the i.v. injection of PepMV-Cy5 and PVX-Cy5, respectively. The mice were euthanized 24 h post injection for ex vivo imaging (Figure 4A), followed by quantitative ROI analysis of the collected organs (Figure 4B). The biodistribution profiles of PepMV and PVX were similar, with particle accumulation in the liver, spleen, and kidney. However, in tumors, PepMV accumulated to 1.5 fold higher levels than PVX and tumors containing PepMV displayed more intense fluorescence than any other organs (e.g., tumor vs liver, $p < 0.01$). The sequestration of nanoparticles including plant VNPs by the spleen and liver was anticipated and indicates clearance by the mononuclear phagocyte system (MPS). We previously observed the profound accumulation of PVX in the spleen (spleen > liver), but this appears to be unique to PVX[25] and does not occur with other VNPs such as CPMV[23] and TMV.[37] Elongated nanoparticles are also expected to undergo renal clearance causing their accumulation in the kidneys because in spite of their length, such VNPs are only ~13 nm in diameter and can align with the blood flow to pass through the glomerular structure with a sub-20 nm size cutoff, followed by absorption within the tubes as previously observed for PVX[38] and synthetic particles such as carbon nanotubes.[39]

For the orthotopic ovarian cancer model, *nu/nu* mice were injected i.p. with luciferase-positive SKOV-3 cells (2×10^6 cells) which are known to metastasize to the ovary, peritoneal wall, and diaphragm and form ascites fluid similar to human ovarian cancer.[40] Luciferase-labeled cells were used to monitor disease progression within the peritoneal cavity. After 40 days, when the disease was established, PepMV-Cy5 or PVX-Cy5 particles (10 mg kg^{-1} body weight) were administered into the i.p. space and images were captured using the IVIS system over the next 72 h (Figure 5A). Although filamentous PepMV and PVX particles could be detected throughout the body (indicating systemic distribution following i.p. administration), the particles were concentrated at the highest levels in the peritoneum. Eventually, the VNPs were cleared from the body by renal clearance via the bladder (indicated by the strong fluorescence in the green circles, Figure 5A). At 36 h post administration, when most PepMV and PVX had been removed from the body, tumor accumulation was indicated by the fluorescent signals from PepMV and PVX (indicated by white arrows) colocalizing with the luminescence of the tumor cells (Figure 5A). Tumor retention was apparent for at least 72 h post administration (Figure 5A). After 72 h, mice were euthanized for ex vivo imaging. Figure 5B confirms the tumor homing of both VNPs, consistent with the in vivo imaging in Figure 5A. Accumulation in organs of the reticuloendothelial system (spleen, liver and kidneys) was also observed (Figure 5B). From ROI analysis, PVX and PepMV generated similar signals in the spleen, kidneys, and liver, with the latter accumulating the most particles in each case (Figure 5C). There were no apparent differences between PepMV and PVX in these organs. It was interesting to note

that in this mouse model, PVX is not preferentially sequestered in the spleen. Similar to the TNBC model, PepMV-treated animals showed double the fluorescence intensity in the tumor compared to that in animals treated with PVX.

Despite the differences in the tumor homing efficiency, both PepMV and PVX were found to accumulate in tumors, as previously reported for other nanoparticles with a high aspect ratio.[22,25] This “passive” tumor homing after systemic administration can be explained by the enhanced permeability and retention (EPR) effect, a unique phenomenon in solid tumors, where tumor hypervascularization results in gaps between endothelial cells allowing the extravasation of nanoscale objects. The lack of lymphatic drainage leads to the retention of these Rodmaterials. Rod-shaped and filamentous nanoparticles show enhanced tumor homing via EPR because they tend to evade phagocytosis and thus have prolonged circulation times, leading to more efficient tumor accumulation. In addition, the enhanced margination and better tissue penetration of elongated VNPs may also facilitate efficient extravasation to tumors.[29] However, EPR-based delivery is significantly influenced by the tumor microenvironment and there is heterogeneity in the comparison of various tumor types, sizes, tissues of origin, primary vs metastatic sites, and/or patient conditions, resulting in case-to-case differences in the outcome of systemic administration.[41] Local delivery via the i.p. route might offer an effective alternative strategy for the treatment of peritoneal malignancies. For example, in ovarian cancer, primary and metastatic tumors are frequently restricted to the peritoneal cavity, allowing direct exposure to treatments by i.p. injection.[42] In addition, nanoparticle-based delivery prevents the rapid diffusion of small payloads into circulation systems following i.p. administration and thus enhances local drug concentrations (Figure 5A), thus increasing tumor exposure and accumulation.[43] Recently, we demonstrated enhanced retention times for spherical CPMV particles within the peritoneum following i.p. injection, improving the efficacy of treatment in the immunocompetent ID8 ovarian cancer model.[44] Here, the fluorescence of i.p. injected PepMV and PVX was confined within the i.p. space up to 72 h post administration, indicating slower clearance rates. The quantity of particles in ovarian tumors were an order of magnitude higher compared to VNP accumulation in the breast cancer model after i.v. delivery (24 h post administration) (Figures 4B and 5C). This may indicate the effective tumor homing of elongated VNPs following i.p. administration targeting ovarian cancer.

PepMV showed a 1.5-fold increase in tumor homing in the MDA-MB-231 mouse model compared to PVX and a 2-fold increase in the SKOV-3 model (Figures 4B and 5C). The biodistribution and tumor homing properties of PepMV and PVX may differ because of their surface charges, surface hydrophilicity/hydrophobicity, and protein—protein interactions. The surface electrostatic potential of PepMV and PVX was estimated in silico using the Bluues server based on the generalized Born model.[36] Overall, the assembled PepMV and PVX CPs have negatively charged surfaces (Figures 1E,F). However, the protein corona, here defined as the outermost protein layer that would interface with the biological milieu, comprises the first 20 amino acid residues of each CP, which is flexible and exposed to the solvent. This is not shown in the model due to the lack of electron density, reflecting its flexible and disordered state. When we consider these flexible arms, structural differences can be detected (Supporting Information, Table S1), which may explain the differences observed in vivo. The PepMV sequence (PDB 5FN1) contains two negatively charged

aspartic acid residues (Asp 3 and Asp 19) and the positively charged Lys 18, whereas PVX (NCBI AAV27212.1) contains only one charged amino acid: Lys 20 (see Supporting Information). Overall, the PepMV corona is slightly negative (−1.2) whereas the PVX corona is slightly positive (0.8) at pH 7.4 as determined using the Protein Calculator tool (http://protcalc.sourceforge.net). Regarding the hydrophobic nature of these peptide tails, PepMV has a GRAVY score of −0.33 compared to −0.45 for PVX, indicating that both peptide tails are hydrophilic. However, the hydropathy plots indicate that the outermost N-terminal portion of PepMV is hydrophilic whereas the equivalent part of PVX is hydrophobic (Supporting Information, Figure S1). These differences may influence the opsonization on the nanoparticles in which hydrophobic surfaces are more prone to protein adsorption for clearance by the reticuloendothelial system.[45] Furthermore, the amino acid compositions of PepMV and PVX are distinct and these subtle differences in the surface chemistry may explain the enhanced tumor homing of PepMV compared to PVX. Future work is required to systematically investigate the structure—function relationship between the charge, hydrophobicity, and/or protein composition of plant VNPs, because these properties can be tuned by surface modification, e.g., by chemical conjugation using polyethylene glycol or zwitterionic polymers or by genetic engineering to tailor the amino acid sequences.

CONCLUSIONS

In conclusion, this work expands the toolbox of filamentous VNPs by establishing PepMV as a nanotechnology platform for drug delivery and bioimaging applications. PepMV is a *Potexvirus* measuring 510 × 13 nm, which is similar to the established platform based on PVX. PepMV has multiple surface-exposed Lys residues, and a bioconjugation procedure for the addition of dyes and other molecules via amine-NHS coupling has been established, allowing the preparation of a high-payload nanoplatform. PepMV can carry up to 1600 chemical modifiers per particle. In mouse models of TNBC and ovarian cancer, up to twice as much PepMV accumulated within the tumor compared to PVX, indicating better tumor homing despite the similar size and shape. These promising findings suggest that PepMV-based nanotechnologies could be developed for multiple biomedical applications.

Supplementary Material

Refer to Web version on PubMed Central for supplementary material.

ACKNOWLEDGMENTS

This work was supported in part by a Research Scholar Award from the American Cancer Society (128319-RSG-15-144-01-CDD to NFS) and a grant from the National Institutes of Health (R01CA202814 to NFS). The Spanish team acknowledges funding from MINECO, Spain (AGL2012-37390, AGL2015-65838-R).

REFERENCES

(1). Wolfbeis OS An Overview of Nanoparticles Commonly Used in Fluorescent Bioimaging. Chem. Soc. Rev. 2015, 44 (14), 4743–4768. [PubMed: 25620543]

(2). Blanco E; Shen H; Ferrari M Principles of Nanoparticle Design for Overcoming Biological Barriers to Drug Delivery. Nat. Biotechnol. 2015, 33 (9), 941–951. [PubMed: 26348965]

(3). Wen AM; Steinmetz NF Design of Virus-Based Nanomaterials for Medicine, Biotechnology, and Energy. Chem. Soc. Rev. 2016, 45 (15), 4074–4126. [PubMed: 27152673]

(4). Schwarz B; Douglas T Development of Virus-Like Particles for Diagnostic and Prophylactic Biomedical Applications. Wiley Interdiscip. Rev. Nanomed. Nanobiotechnol. 2015, 7 (5), 722–735. [PubMed: 25677105]

(5). Aljabali AA; Shukla S; Lomonossoff GP; Steinmetz NF; Evans DJ Cpmv-Dox Delivers. Mol. Pharmaceutics 2013, 10 (1), 3–10.

(6). Leong HS; Steinmetz NF; Ablack A; Destito G; Zijlstra A; Stuhlmann H; Manchester M; Lewis JD Intravital Imaging of Embryonic and Tumor Neovasculature Using Viral Nanoparticles. Nat. Protoc. 2010, 5 (8), 1406–1417. [PubMed: 20671724]

(7). Taylor KM; Lin T; Porta C; Mosser AG; Giesing HA; Lomonossoff GP; Johnson JE Influence of Three-Dimensional Structure on the Immunogenicity of a Peptide Expressed on the Surface of a Plant Virus. J. Mol. Recognit. 2000, 13 (2), 71–82. [PubMed: 10822251]

(8). Lizotte PH; Wen AM; Sheen MR; Fields J; Rojanasopondist P; Steinmetz NF; Fiering S Situ Vaccination with Cowpea Mosaic Virus Nanoparticles Suppresses Metastatic Cancer. Nat. Nanotechnol. 2016, 11 (3), 295–303. [PubMed: 26689376]

(9). Zeng Q; Wen H; Wen Q; Chen X; Wang Y; Xuan W; Liang J; Wan S Cucumber Mosaic Virus as Drug Delivery Vehicle for Doxorubicin. Biomaterials 2013, 34 (19), 4632–4642. [PubMed: 23528229]

(10). Masarapu H; Patel BK; Chariou PL; Hu H; Gulati NM; Carpenter BL; Ghiladi RA; Shukla S; Steinmetz NF Physalis Mottle Virus-Like Particles as Nanocarriers for Imaging Reagents and Drugs. Biomacromolecules 2017, 18 (12), 4141–4153. [PubMed: 29144726]

(11). Cao J; Guenther RH; Sit TL; Opperman CH; Lommel SA; Willoughby JA Loading and Release Mechanism of Red Clover Necrotic Mosaic Virus Derived Plant Viral Nanoparticles for Drug Delivery of Doxorubicin. Small 2014, 10 (24), 5126–5136. [PubMed: 25098668]

(12). Vernekar AA; Berger G; Czapar AE; Veliz FA; Wang DI; Steinmetz NF; Lippard SJ Speciation of Phenanthriplatin and Its Analogs in the Core of Tobacco Mosaic Virus. J. Am. Chem. Soc. 2018, 140 (12), 4279–4287. [PubMed: 29553267]

(13). Czapar AE; Zheng YR; Riddell IA; Shukla S; Awuah SG; Lippard SJ; Steinmetz NF Tobacco Mosaic Virus Delivery of Phenanthriplatin for Cancer Therapy. ACS Nano 2016, 10 (4), 4119–4126. [PubMed: 26982250]

(14). Franke CE; Czapar AE; Patel RB; Steinmetz NF Tobacco Mosaic Virus-Delivered Cisplatin Restores Efficacy in Platinum-Resistant Ovarian Cancer Cells. Mol. Pharmaceutics 2018, 15 (8), 2922–2931.

(15). Hu H; Zhang Y; Shukla S; Gu Y; Yu X; Steinmetz NF Dysprosium-Modified Tobacco Mosaic Virus Nanoparticles for Ultra-High-Field Magnetic Resonance and near-Infrared Fluorescence Imaging of Prostate Cancer. ACS Nano 2017, 11 (9), 9249–9258. [PubMed: 28858475]

(16). Bruckman MA; Jiang K; Simpson EJ; Randolph LN; Luyt LG; Yu X; Steinmetz NF Dual-Modal Magnetic Resonance and Fluorescence Imaging of Atherosclerotic Plaques in Vivo Using Vcam-1 Targeted Tobacco Mosaic Virus. Nano Lett. 2014, 14 (3), 1551–1558. [PubMed: 24499194]

(17). Koo M; Bendahmane M; Lettieri GA; Paoletti AD; Lane TE; Fitchen JH; Buchmeier MJ; Beachy RN Protective Immunity against Murine Hepatitis Virus (Mhv) Induced by Intranasal or Subcutaneous Administration of Hybrids of Tobacco Mosaic Virus That Carries an Mhv Epitope. Proc. Natl. Acad. Sci. U. S. A. 1999, 96 (14), 7774–7779. [PubMed: 10393897]

(18). Staczek J; Bendahmane M; Gilleland LB; Beachy RN; Gilleland HE Jr Immunization with a Chimeric Tobacco Mosaic Virus Containing an Epitope of Outer Membrane Protein F of Pseudomonas Aeruginosa Provides Protection against Challenge with P. Aeruginosa. Vaccine 2000, 18 (21), 2266–2274. [PubMed: 10717347]

(19). Jiang L; Li Q; Li M; Zhou Z; Wu L; Fan J; Zhang Q; Zhu H; Xu Z A Modified Tmv-Based Vector Facilitates the Expression of Longer Foreign Epitopes in Tobacco. Vaccine 2006, 24(2), 109–115. [PubMed: 16337317]

(20). Murray AA; Wang C; Fiering S; Steinmetz NF Situ Vaccination with Cowpea Vs Tobacco Mosaic Virus against Melanoma. Mol. Pharmaceutics 2018, 15 (9), 3700–3716.

(21). Le DH; Lee KL; Shukla S; Commandeur U; Steinmetz NF Potato Virus X, a Filamentous Plant Viral Nanoparticle for Doxorubicin Delivery in Cancer Therapy. Nanoscale 2017, 9 (6), 2348–2357. [PubMed: 28144662]

(22). Shukla S; Dickmeis C; Nagarajan AS; Fischer R; Commandeur U; Steinmetz NF Molecular Farming of Fluorescent Virus-Based Nanoparticles for Optical Imaging in Plants, Human Cells and Mouse Models. Biomater. Sci 2014, 2 (5), 784–797.

(23). Shukla S; Ablack AL; Wen AM; Lee KL; Lewis JD; Steinmetz NF Increased Tumor Homing and Tissue Penetration of the Filamentous Plant Viral Nanoparticle Potato Virus X. Mol. Pharmaceutics 2013, 10 (1), 33–42.

(24). Lee KL; Murray AA; Le DHT; Sheen MR; Shukla S; Commandeur U; Fiering S; Steinmetz NF Combination of Plant Virus Nanoparticle-Based in Situ Vaccination with Chemotherapy Potentiates Antitumor Response. Nano Lett. 2017, 17 (7), 4019–4028. [PubMed: 28650644]

(25). Shukla S; Wen AM; Ayat NR; Commandeur U; Gopalkrishnan R; Broome AM; Lozada KW; Keri RA; Steinmetz NF Biodistribution and Clearance of a Filamentous Plant Virus in Healthy and Tumor-Bearing Mice. Nanomedicine (London, U. K.) 2014, 9 (2), 221–235.

(26). Zhang W; Zhang Z; Zhang Y The Application of Carbon Nanotubes in Target Drug Delivery Systems for Cancer Therapies. Nanoscale Res. Lett. 2011, 6, 555. [PubMed: 21995320]

(27). Christian DA; Cai S; Garbuzenko OB; Harada T; Zajac AL; Minko T; Discher DE Flexible Filaments for in Vivo Imaging and Delivery: Persistent Circulation of Filomicelles Opens the Dosage Window for Sustained Tumor Shrinkage. Mol. Pharmaceutics 2009, 6 (5), 1343–1352.

(28). Toy R; Peiris PM; Ghaghada KB; Karathanasis E Shaping Cancer Nanomedicine: The Effect of Particle Shape on the in Vivo Journey of Nanoparticles. Nanomedicine (London, U. K.) 2014, 9 (1), 121–134.

(29). Kinnear C; Moore TL; Rodriguez-Lorenzo L; Rothen-Rutishauser B; Petri-Fink A Form Follows Function: Nanoparticle Shape and Its Implications for Nanomedicine. Chem. Rev. 2017, 117 (17), 11476–11521. [PubMed: 28862437]

(30). Meyer RA; Green JJ Shaping the Future of Nanomedicine: Anisotropy in Polymeric Nanoparticle Design. Wiley Interdiscip. Rev. Nanomed. Nanobiotechnol 2016, 8 (2), 191–207. [PubMed: 25981390]

(31). Hanssen IM; Thomma BP Pepino Mosaic Virus: A Successful Pathogen That Rapidly Evolved from Emerging to Endemic in Tomato Crops. Mol. Plant Pathol. 2010, 11 (2), 179–189. [PubMed: 20447268]

(32). Sempere RN; Gomez P; Truniger V; Aranda MA Development of Expression Vectors Based on Pepino Mosaic Virus. Plant Methods 2011, 7, 6. [PubMed: 21396092]

(33). Agirrezabala X; Mendez-Lopez E; Lasso G; Sanchez-Pina MA; Aranda M; Valle M The near-Atomic Cryoem Structure of a Flexible Filamentous Plant Virus Shows Homology of Its Coat Protein with Nucleoproteins of Animal Viruses. eLife 2015, 4, No. e11795. [PubMed: 26673077]

(34). Le DHT; Hu H; Commandeur U; Steinmetz NF Chemical Addressability of Potato Virus X for Its Applications in Bio/Nanotechnology. J. Struct. Biol. 2017, 200 (3), 360–368. [PubMed: 28647539]

(35). Lee KL; Uhde-Holzem K; Fischer R; Commandeur U; Steinmetz NF Genetic Engineering and Chemical Conjugation of Potato Virus X. Methods Mol. Biol. 2014, 1108, 3–21. [PubMed: 24243237]

(36). Walsh I; Minervini G; Corazza A; Esposito G; Tosatto SC; Fogolari F Bluues Server: Electrostatic Properties of Wild-Type and Mutated Protein Structures. Bioinformatics 2012, 28 (16), 2189–2190. [PubMed: 22711791]

(37). Bruckman MA; Randolph LN; VanMeter A; Hern S; Shoffstall AJ; Taurog RE; Steinmetz NF Biodistribution, Pharmacokinetics, and Blood Compatibility of Native and Pegylated Tobacco Mosaic Virus Nano-Rods and -Spheres in Mice. Virology 2014,449, 163–173. [PubMed: 24418549]

(38). Lee KL; Shukla S; Wu M; Ayat NR; El Sanadi CE; Wen AM; Edelbrock JF; Pokorski JK; Commandeur U; Dubyak GR; Steinmetz NF Stealth Filaments: Polymer Chain Length and Conformation Affect the in Vivo Fate of Pegylated Potato Virus X. Acta Biomater. 2015, 19, 166–179. [PubMed: 25769228]

(39). Ruggiero A; Villa CH; Bander E; Rey DA; Bergkvist M; Batt CA; Manova-Todorova K; Deen WM; Scheinberg DA; McDevitt MR Paradoxical Glomerular Filtration of Carbon Nanotubes. Proc. Natl. Acad. Sci. U. S. A. 2010, 107 (27), 12369–12374. [PubMed: 20566862]

(40). Bobbs AS; Cole JM; Cowden Dahl KD Emerging and Evolving Ovarian Cancer Animal Models. Cancer Growth Metastasis 2015,8, 29–36. [PubMed: 26380555]

(41). Prabhakar U; Maeda H; Jain RK; Sevick-Muraca EM; Zamboni W; Farokhzad OC; Barry ST; Gabizon A; Grodzinski P; Blakey DC Challenges and Key Considerations of the Enhanced Permeability and Retention Effect for Nanomedicine Drug Delivery in Oncology. Cancer Res. 2013, 73 (8), 2412–2417. [PubMed: 23423979]

(42). Scarlett UK; Cubillos-Ruiz JR; Nesbeth YC; Martinez DG; Engle X; Gewirtz AT; Ahonen CL; Conejo-Garcia JR Situ Stimulation of Cd40 and Toll-Like Receptor 3 Transforms Ovarian Cancer-Infiltrating Dendritic Cells from Immunosuppressive to Immunostimulatory Cells. Cancer Res. 2009, 69 (18), 7329–7337. [PubMed: 19738057]

(43). Dakwar GR; Shariati M; Willaert W; Ceelen W; De Smedt SC; Remaut K Nanomedicine-Based Intraperitoneal Therapy for the Treatment of Peritoneal Carcinomatosis - Mission Possible? Adv. Drug Delivery Rev. 2017, 108, 13–24.

(44). Czapar AE; Tiu BDB; Veliz FA; Pokorski JK; Steinmetz NF Slow-Release Formulation of Cowpea Mosaic Virus for in Situ Vaccine Delivery to Treat Ovarian Cancer. Adv. Sci. 2018, 5 (5), 1700991.

(45). Duan X; Li Y Physicochemical Characteristics of Nano-particles Affect Circulation, Biodistribution, Cellular Internalization, and Trafficking. Small 2013, 9 (9–10), 1521–1532. [PubMed: 23019091]

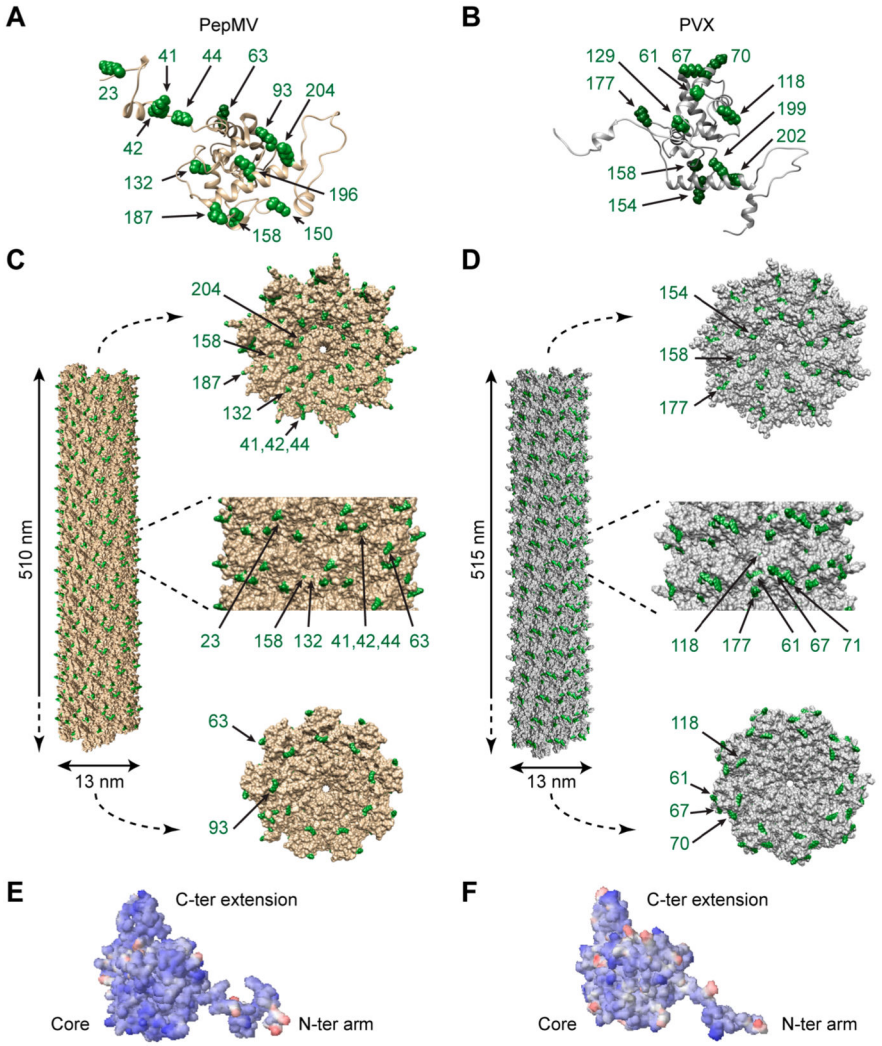

Figure 1.

Structural models of PepMV and PVX. The atomic models of (A) PepMV and (B) PVX coat protein (CP) subunits highlighting lysine side chains (Lys, green). Representation of a portion of the helical assemblies of (C) PepMV and (D) PVX CP (300 subunits). Views from different angles (top view, side view, and bottom view) indicate surface-exposed Lys (green). Surface electrostatic potentials of the atomic structures of (E) PepMV and (F) PVX. Negatively charged, neutral, and positively charged surfaces are shown in blue, white, and red, respectively.

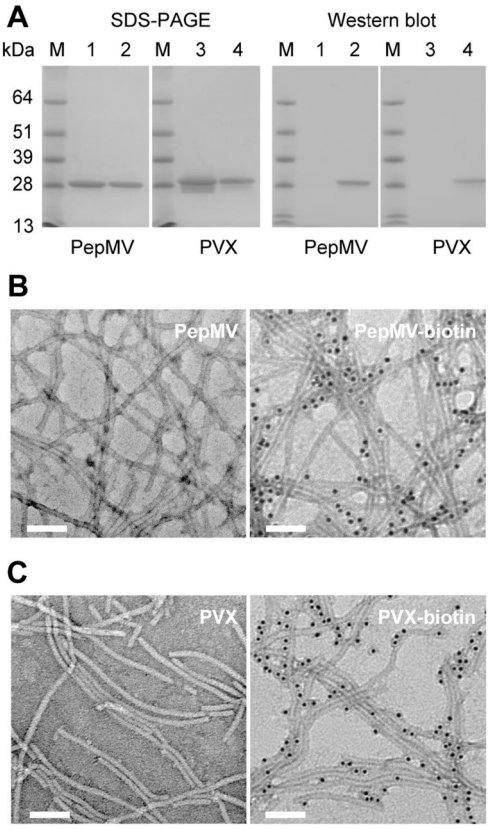

Figure 2.

Characterization of PepMV-biotin and PVX-biotin conjugates. (A) Gel electrophoresis (SDS-PAGE) and Western blot analysis of (1) PepMV control vs (2) PepMV-biotin, (3) PVX control, and (4) PVX-biotin. M: SeeBlue Plus2 Protein Standards. (B, C) TEM images of immunogold stained (B) nonmodified PepMV and PepMV-biotin and (C) nonmodified PVX and PVX-biotin. Scale bars = 100 nm.

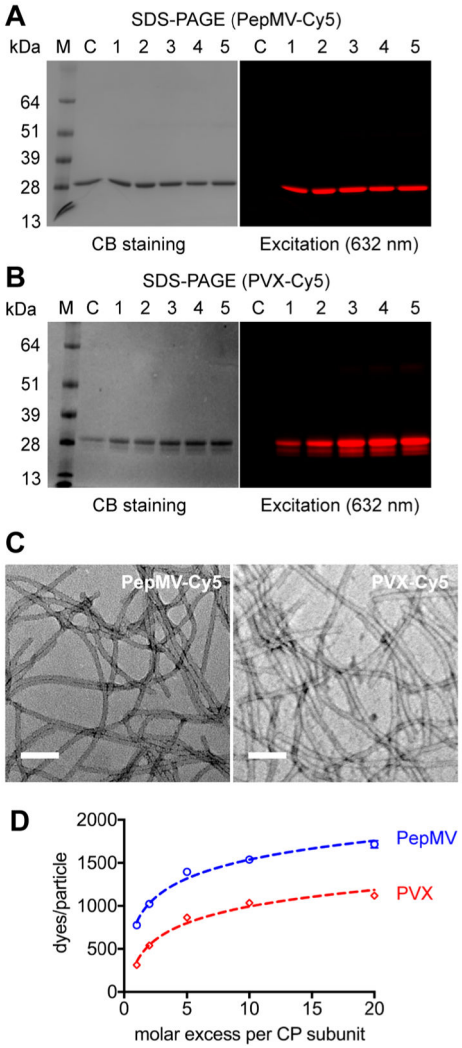

Figure 3.

Characterization of fluorescence-labeled PepMV-Cy5 and PVX-Cy5. SDS-PAGE analysis of (A) PepMV-Cy5 and (B) PVX-Cy5 at increasing molar excesses of sulfo-Cy5-NHS in the reaction mixtures. (1–5) CP/dye molar ratio: 1:1, 1:2, 1:5, 1:10, 1:20, C/nonlabeled particles as controls. (C) The filamentous structures of PepMV-Cy5 and PVX-Cy5 after modification and purification. Scale bars = 100 nm. (D) The number of attached Cy5 molecules per particle (PepMV or PVX) as a function of the molar excess of dye. Experiments were carried out in triplicate, values are shown as means ± SD. Error bars are not displayed when their length is smaller than the marker sizes.

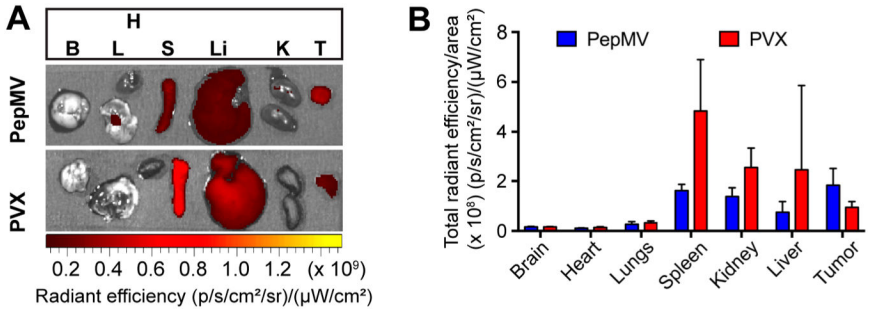

Figure 4.

Biodistribution profiles of PepMV and PVX 24 h post intravenous administration at a dose of 10 mg kg^{-1} in *nu/nu* mice bearing MDA-MB-231 triple negative breast cancer tumors. (A) Ex vivo fluorescence images of excised organs. (B) Quantitative region of interest (ROI) analysis of each organ determined by total radiant efficiency per area. Data are expressed as means ± SD ($n = 3$).

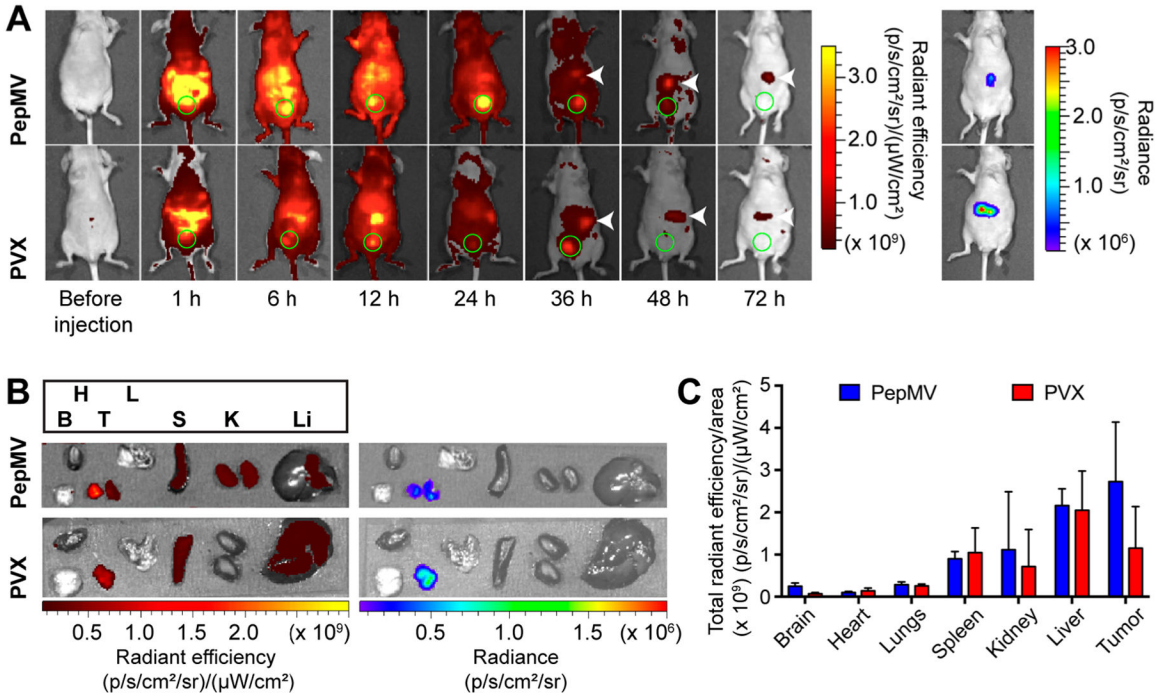

Figure 5.

Biodistribution profiles of PepMV and PVX after intraperitoneal administration at a dose of 10 mg kg^{-1} in *nu/nu* mice bearing SKOV-3/Luc ovarian tumors. (A) Real time in vivo fluorescence images of PepMV and PVX over 72 h. Bladders are indicated by green circles. Tumors within the peritoneum were detected by in vivo bioluminescence imaging. The matched locations are indicated by white arrows in the fluorescence images. (B) Ex vivo fluorescence and luminescence images of excised organs from the mice injected with PepMV or PVX 72 h post administration. (C) Quantitative region of interest (ROI) analysis of each organ determined by total radiant efficiency per area. Data are expressed as means ± SD ($n = 3$).

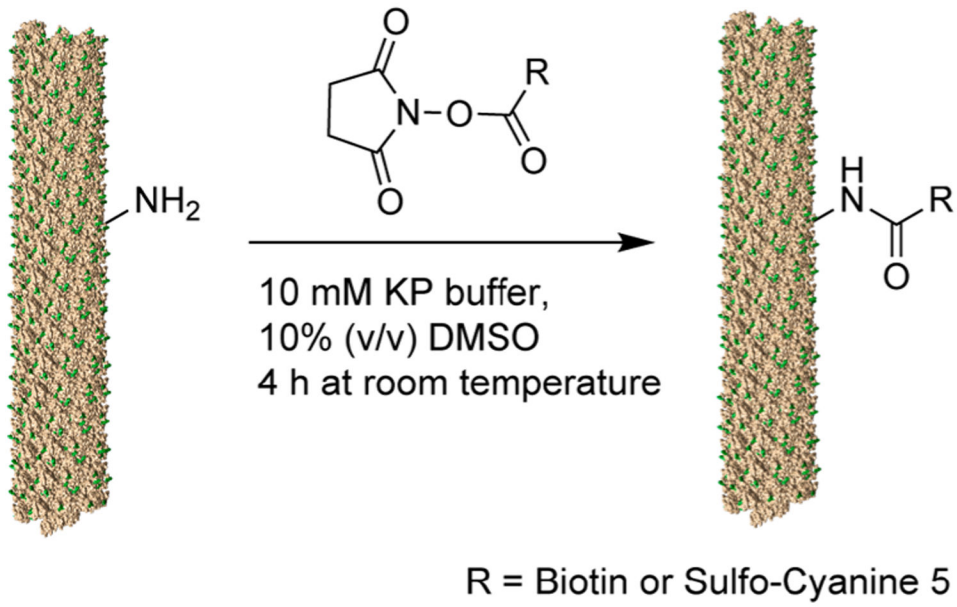

Scheme 1.

Reaction Scheme for the Bioconjugation of PepMV or PVX with a Biotin Tag or the Fluorescent Probe Cy5 Functionalized with the NHS-Handle via an Amine-NHS Coupling Reaction